

# Corrosion Performances of Selective Laser Melting Ti6Al4V Alloy in Different Solutions

Xuedan Chen <sup>1,2</sup>, Qilong Liao <sup>1,\*</sup>, Min Gong <sup>2</sup> and Qingshan Fu <sup>1,3,\*</sup><sup>1</sup> School of Materials and Chemistry, Southwest University of Science and Technology, Mianyang 621010, China<sup>2</sup> College of Material Science and Engineering, Sichuan University of Science and Engineering, Zigong 643000, China<sup>3</sup> Vanadium and Titanium Resource Comprehensive Utilization Key Laboratory of Sichuan Province, Panzhihua 617016, China

\* Correspondence: liaoqilong@swust.edu.cn (Q.L.); sendysan@suse.edu.cn (Q.F.)

**Abstract:** Selective laser melting (SLM) can fabricate titanium and its alloy components with both elaborate internal architectures and complex shapes without geometric constrictions. The corrosion resistance of SLM-produced Ti and its alloy is crucial in some applications such as marine and biomedical environments. Here, potentiodynamic polarization and electrochemical impedance spectroscopy were used to evaluate the corrosion behaviors of SLM-produced Ti-6Al-4V in the four corrosive media (simulated body fluid (SBF), phosphate buffered saline solutions (PBS), 3.5 wt.% NaCl aqueous solution, 15 wt.% NaCl aqueous solution). The relevant results demonstrate the inferior corrosion resistance of the SLM-produced Ti-6Al-4V sheet compared with the commercial casting Ti-6Al-4V sheet in the four solutions. The corrosive current density of SLM-produced Ti-6Al-4V in PBS solution is  $1.78 \mu\text{A cm}^{-2}$  and  $7.065 \mu\text{A cm}^{-2}$  in 15 wt.% NaCl solution, and the values of charge transfer resistance for SLM-produced Ti-6Al-4V in the four solutions are in the order:  $17.9 \text{ k}\Omega \text{ cm}^{-2}$  (in 15 wt.% NaCl) <  $25.2 \text{ k}\Omega \text{ cm}^{-2}$  (in 3.5 wt.% NaCl) <  $28.1 \text{ k}\Omega \text{ cm}^{-2}$  (in SBF) <  $39.8 \text{ k}\Omega \text{ cm}^{-2}$  (in PBS), demonstrating the best protective performance of the passivation film on the SLM-produced Ti-6Al-4V sheet in PBS.

**Keywords:** selective laser melting; Ti alloy; corrosion resistance; PBS; SBF

**Citation:** Chen, X.; Liao, Q.; Gong, M.; Fu, Q. Corrosion Performances of Selective Laser Melting Ti6Al4V Alloy in Different Solutions. *Metals* **2023**, *13*, 192. <https://doi.org/10.3390/met13020192>

Academic Editor: Yugui Zheng

Received: 9 December 2022

Revised: 5 January 2023

Accepted: 13 January 2023

Published: 18 January 2023



**Copyright:** © 2023 by the authors. Licensee MDPI, Basel, Switzerland. This article is an open access article distributed under the terms and conditions of the Creative Commons Attribution (CC BY) license (<https://creativecommons.org/licenses/by/4.0/>).

## 1. Introduction

Titanium (Ti) and its alloys have been used in aerospace, aeronautic, automotive, biomedical, structural, and other applications because of their less density than materials like steel and higher stress support than Al-alloys [1–4]. In some applications, producing Ti and its alloy parts with a high geometrical complexity or specially designed parts for individuals are expected. For instance, in bone loss replacement orthopedic prostheses usually need to fabricate uniform and size-controlled pore structures [5–7]. A variety of methods have been utilized for the fabrication of porous systems, such as sintered beads [8], fiber mesh [9], and thermal spray processes [5], space holder technique [10]. However, they have disadvantages such as compromised microstructure, incapability to achieve interconnected pores at optimal porosity level, lack of porosity controllability, mismatch of mechanical properties between implants and human bone. As such, the advanced rapid prototype technology was coming.

Rapid prototype technology or additive manufacturing (AM) is a process of adding materials layer by layer to make objects from digital 3D models [11–13]. AM is capable of accurately controlling both the internal architecture and complex shape without geometric constrictions. As an important one of AM, selective laser melting (SLM) uses a fiber laser as the energy source and selectively melts powder in an inert gas filled or vacuum chamber which ensures higher purity by minimizing the oxygen in the environment and reducing

the risk of hydrogen pick up [14–16]. With SLM kinds of Ti and its alloy components have been produced successfully [17–21].

With respect to SLM-produced Ti and its alloy components, the present attention is mainly focused on utmost high density or sophisticated structures, expected mechanical properties, preferable microstructures [22–25]. For example, Ti alloy bone repairment implants with elastic constants falling in the range of 1.0 to 25.0 GPa (Human bones' elastic constants) were produced by SLM to avoid “stress shielding” [26,27]. The deliberately fabricated pore structures in the Ti alloy implants reduced the elastic constant from ~110 Gpa to ~20 Gpa. Considering their application environments, such as corrosive chemical solution systems, human body and marine environments, the corrosion resistance of SLM-produced Ti and its alloys is another critical property. So far there have been several studies on the corrosion behaviors of SLM-produced Ti and its alloys. Chiu et al. studied the tribocorrosion of SLM-produced Ti-6Al-4V in Ringer's simulated body solution. The electrochemical characteristics in anodic polarization were similar for the SLM-produced Ti-6Al-4V and traditional fabricated Ti-6Al-4V sheets; both the samples possessed large and steady passivation regions. However, the  $Ti_3O$  and  $Ti_6O$  phases in the SLM-produced Ti-6Al-4V parts led to a superior wear resistance compared with traditional fabricated Ti-6Al-4V [17]. The corrosion behavior of SLM-produced Ti-6Al-4V alloy in NaCl solution was also evaluated, and the critical potentials ( $E_{cp}$ ) of the commercial Grade 5 alloy and SLM-produced Ti-6Al-4V were compared. The value of  $E_{cp}$  is usually used to describe the stability of the film on the surface of metal. The greater the value of  $E_{cp}$ , the more stable the passive film. The greater value of  $E_{cp}$  in the commercial Grade 5 alloy indicated that the SLM-produced Ti-6Al-4V sample exhibited a worse corrosion resistance, and its unfavorable corrosion resistance was attributed to the dominant  $\alpha'$  and less  $\beta$ -Ti [19]. Cui et al. discovered the metastable pitting corrosion behavior of SLM-produced Ti-6Al-4V in Hank's solution, and concluded that the passive films formed on the sample exhibited a higher flux of oxygen vacancies, resulting in the absorption of more aggressive ions, thereby producing more cation vacancies [21]. In this work, given the practical applications of Ti alloys, we chose four different solutions (simulated body fluid (SBF), phosphate buffered saline solutions (PBS), 3.5 wt.% NaCl aqueous solution, 15 wt.% NaCl aqueous solution) as corrosion media to evaluate the corrosion resistance of SLM-manufactured Ti-6Al-4V.

## 2. Materials and Methods

### 2.1. Materials

Ti-6Al-4V alloy powder with the particle size of 15–45  $\mu\text{m}$  was purchased from commercial route. Sodium chloride (NaCl), sodium bicarbonate ( $\text{NaHCO}_3$ ), potassium chloride (KCl), dipotassium hydrogen phosphate trihydrate ( $\text{K}_2\text{HPO}_4 \cdot 3\text{H}_2\text{O}$ ) and magnesium chloride hexahydrate ( $\text{MgCl}_2 \cdot 6\text{H}_2\text{O}$ ), calcium chloride dihydrate ( $\text{CaCl}_2 \cdot 2\text{H}_2\text{O}$ ), sodium sulfate ( $\text{Na}_2\text{SO}_4$ ) HCl solution (37%) were bought from Kelong Company (Chengdu, China). Deionized water was used as needed.

### 2.2. Preparation of Samples

Here, the selective laser melting (SLM) was employed to fabricate Ti alloy sheets (20 mm  $\times$  20 mm  $\times$  1.5 mm) in a MTT SLM 250 HL machine containing a 400 W Yb:YAG fiber laser with an 80  $\mu\text{m}$  spot size. The SLM-produced samples were manufactured using a laser power (at the part bed) of 200 W ( $\lambda = 1.07 \mu\text{m}$ ) and laser scan speeds of 1250 mm/s. Both the hatch spacing (distance between scan lines) and the layer thickness were 100  $\mu\text{m}$ . The direction of scanning was rotated of 90° between successive layers. The shape and size of the SLM-produced Ti-6Al-4V (noted as ST) sheet and commercial Ti-6Al-4V (noted as CT) sheets were illustrated in Figure 1. The density of ST was determined the value > 99% using the Archimedes method. Table 1 lists the chemical compositions of ST and CT, which indicates that the compositions of the two samples are similar. In order to evaluate their electrochemical properties, the samples were embedded in epoxy resin, and

the surfaces were mechanically abraded with silica carbide paper up to 2000 grit, and then were ultrasonically cleaned in deionized water, rinsed in ethanol and dried in cool air.

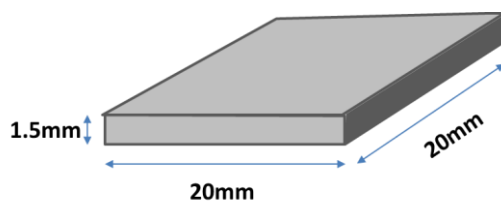


**Figure 1.** Size parameters of prepared titanium sheets.

**Table 1.** Chemical composition (wt.%) of Commercial Casting Ti-6Al-4V and SLM-produced Ti-6Al-4V.

|    | C    | H     | O    | N     | Fe   | Al   | V    | Ti   |
|----|------|-------|------|-------|------|------|------|------|
| ST | 0.01 | 0.015 | 0.19 | 0.021 | 0.23 | 6.15 | 4.03 | Bal. |
| CT | 0.02 | 0.001 | 0.11 | 0.016 | 0.53 | 6.18 | 4.04 | Bal. |

### 2.3. Electrochemical Measurement

Electrochemical measurements including open circuit potential (OCP), potentiodynamic polarization and electrochemical impedance spectroscopy (EIS) were conducted using a SolartronSI1280 electrochemical station in a conventional three-electrode cell. The working electrode was the as-prepared commercial and SLM-produced Ti-6Al-4V samples with an exposed apparent surface area of 4 cm<sup>2</sup>. A platinum sheet was used as counter electrode and a saturated calomel electrode (SCE) as the reference electrode. SBF, PBS, 3.5 wt.% NaCl solution, 15 wt.% NaCl solution and were utilized as the electrolytes. SBF and PBS were prepared according to the processes reported in the literatures [28,29]. Prior to the polarization and EIS tests, the samples were kept in the electrolyte for enough time to attain a stable OCP. The potentiodynamic polarization curves were performed from the potential range of  $-0.5$  to  $1.0$  V versus OCP at a sweep rate of 1 mV/s. EIS was performed at the OCP potentiostatically. The frequency range for EIS was from 100 kHz to 10 mHz with an amplitude of 5 mV. All reported potentials in this work were relative to SCE, and the electrochemical measurements were carried out at the temperature of  $25 \pm 1$  °C. The Zview 3.4 and VersaStudio 2.1 softwares were used to determine the EIS curve fitting and corrosion rate, respectively. Triplicate experiments were carried out for all samples to ensure reproducibility.

### 2.4. Characterization of Samples

The morphology of SLM-fabricated sample and commercial Ti-6Al-4V sheet were evaluated by Scanning Electron Microscopy (SEM, S-4800, Hitachi, Tokyo, Japan). The elements in the samples were analyzed by energy-dispersive X-ray Spectroscopy (EDS, JSM-5610LV, JEOL, Tokyo, Japan). The phase constituents of the samples were examined by X-ray diffraction (D8Advance, Bruker, Karlsruhe, Germany) using Cu K $\alpha$  radiation with  $2\theta$  ranging from  $15^\circ$  to  $100^\circ$  at room temperature. An optical microscope (GX51, Olympus, Tokyo, Japan) was used to further distinguish the microstructural difference between ST and CT. As for microstructural studies, the specimens were etched in a Kroll's solution consisting of 10 mL HF, 15 mL HNO<sub>3</sub> and 75 mL H<sub>2</sub>O.

## 3. Results and Discussion

### 3.1. Characterization of the Samples

The SEM images of ST and CT are show in Figure 2A,B,D,E. Accordingly, ST and CT show the obviously different microstructures. In the ST sheet, white  $\beta$  layer phase is arranged in bundles, which separates the gray  $\alpha'$  phase. Some tiny holes can be found in the gap between the parallel  $\beta$  layers. These micropores may weaken the corrosion resistance

of the titanium sheet. In contrast, in the CT sheet the  $\beta$  layers are thicker and the micropore structures are less common than in CT. The phase compositions in the two samples were clearly distinguished by etching and optical microscope observation. A typical acicular-like  $\alpha'$  phase martensitic microstructure in ST could be found (Figure 2G), which was mainly caused by the fast-cooling rate in the SLM process. The CT sheet presents a dual-phase structure with  $\alpha + \beta$  phases (Figure 2H). Compared with Electron beam melting (EBM), another typical additive manufacturing technology, the EBM Ti-6Al-4V alloy is generally characterized by a predominant  $\alpha$  phase from diffusion-controlled phase transformation and small amount of residual  $\beta$ , giving rise to distinct microstructure compared to its SLM counterpart [30–32].

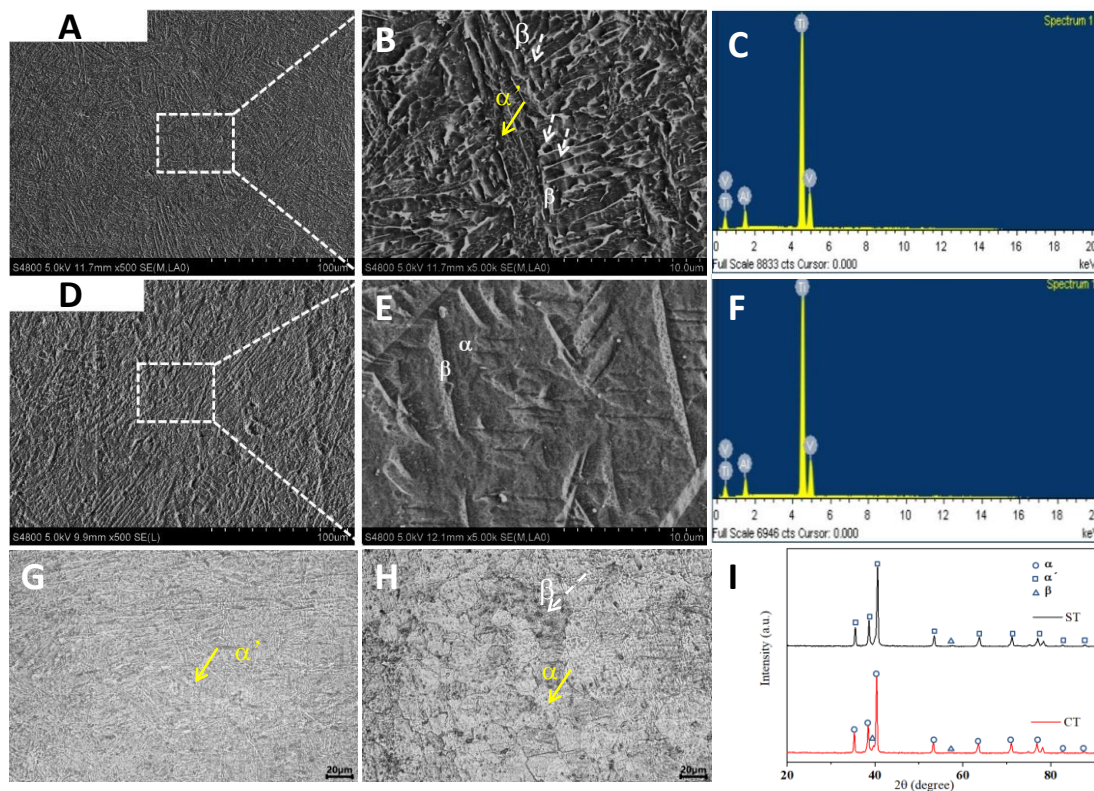


**Figure 2.** SEM images of (A,B) ST and (D,E) CT; EDS spectrum of (C) ST and (F) CT; optical images of (G) ST, (H) CT; (I) XRD patterns for the two samples.

The XRD test further evaluates the phase composition of the samples. ST primarily consists of  $\alpha'$  phase, while  $\alpha$  phase is dominant in CT. The peaks of  $\alpha$  and  $\alpha'$  phases are almost coincident in the XRD pattern (Figure 2I), so it is difficult to distinguish  $\alpha'$  and  $\alpha$  phases simply in terms of the results of XRD. According to the EDS spectrum (Figure 2C,F) of the two samples, elemental composition can be acquired as: Al-8.6%, Ti-87.2%, V-4.2% in ST and Al-8.29%, Ti-87.44%, V-4.27% in CT. Obviously, the two materials have the same chemical composition. Based on the above results, the following conclusions can be drawn: SLM-produced Ti-6Al-4V and Commercial Casting Ti-6Al-4V have the same chemical composition, but their metallographic microstructures are different. This conclusion has been demonstrated by several previous research [21,33].

### 3.2. Electrochemical Studies

To discover the corrosive performance of SLM-produced titanium sheets in plausible applicational environments (such as marine and biomedical applications), here four solutions were used as corrosion media. NaCl solutions with different concentrations were employed to simulate the systems containing different contents of  $\text{Cl}^-$ ; PBS buffer solution

was utilized to mimic the ion concentration, osmolarity, and pH of human body fluids; SBF was employed to imitate the ion concentration of human blood plasma.

The potentiodynamic polarization curves of ST and CT in the four solutions (3.5 wt.% NaCl solution, 15 wt.% NaCl solution, PBS and SBF) are shown in Figure 3. Before polarization tests, the samples were allowed sufficient time to achieve a stable OCP value. According to Figure 3A, the anode regions of the polarization curves of ST and CT in 3.5 wt.% NaCl solution present the characteristics of metal passivation. The initiating passive potential of ST (0.279 V) is greater than that of CT (0.020 V), which manifests that CT is more easily in formation of passivation film. In addition, CT also has the lower passive current density than ST. This suggests that CT is more prone to passivation than ST. During the passivation process, CT exhibits the inferior maintaining passivity current density. Generally, the maintaining passivity current density is directly proportional to the corrosion rate of a metal after passivation. The smaller maintaining passivity current density of CT illustrates the passivation film formed on the surface of CT had better protection performance, that is, the corrosion resistance of CT in 3.5 wt.% NaCl solution is better than that of ST. When in the 15 wt.% NaCl solution, both ST and CT do not show obvious passive features in the anode polarization region of the polarization curves (Figure 3B). This indicates that with the increase of  $\text{Cl}^-$  concentration, the passivation film on the metal surface was locally destroyed, which makes the metal activated and leads to the disappearance of the anode passivation zone. From Figure 3C,D, it can be seen both ST and CT have obvious passivation in the PBS and SBF solutions. The initiating passive potential and passive current density of ST are higher than that of CT, demonstrating that the corrosion resistance of CT in the two systems is better than that of ST.

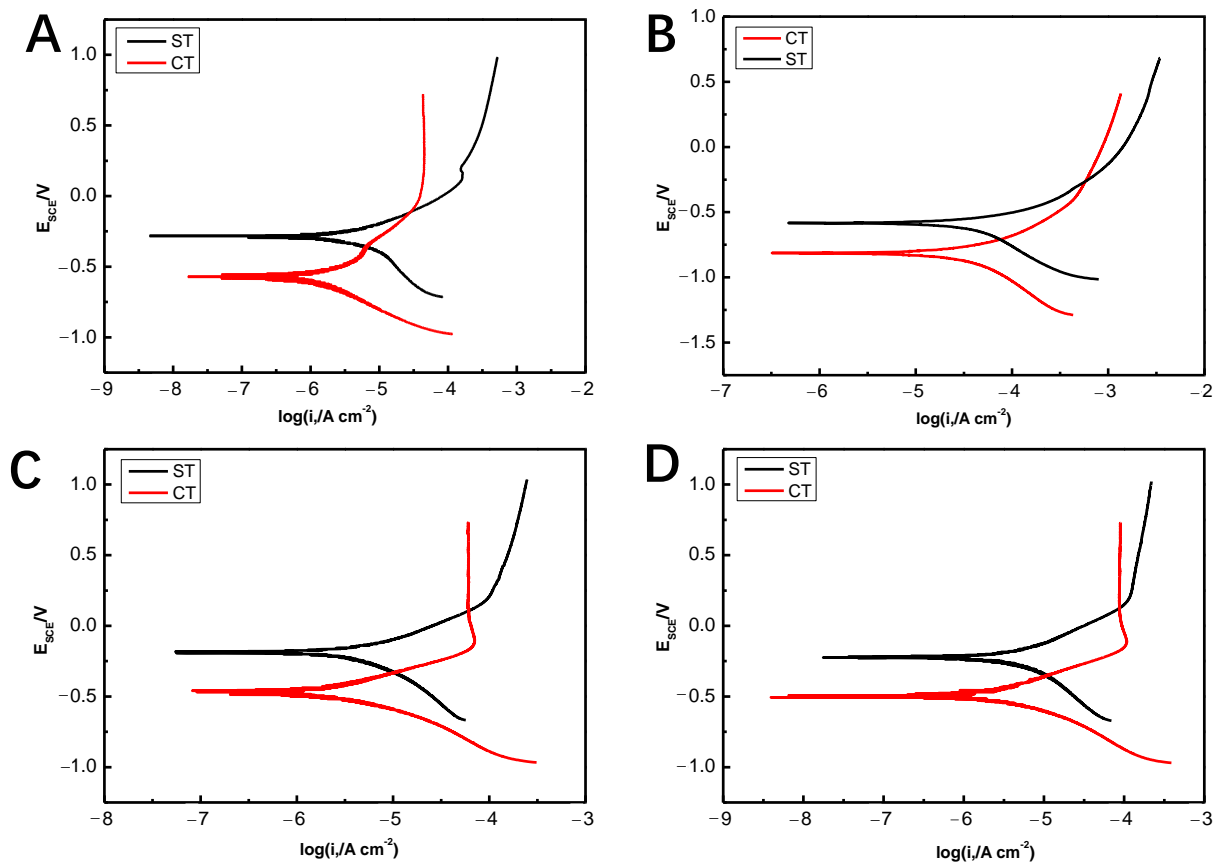


**Figure 3.** Potentiodynamic curves for ST and CT in (A) 3.5 wt.% NaCl solution, (B) 15 wt.% NaCl solution, (C) PBS buffer solution and (D) SBF solution.

The fitting results of potentiodynamic polarization tests for ST and CT in the four solutions are listed in Table 2. The corrosion resistance of ST was the best in PBS solution ( $j_{\text{corr}} = 1.78 \mu\text{A cm}^{-2}$ ), and the lowest in 15 wt.% NaCl solution ( $j_{\text{corr}} = 7.065 \mu\text{A cm}^{-2}$ ). This may be due to the pores in the passivation film on the surface of ST, in which  $\text{Cl}^-$  in the solution would be accumulated, causing the local rupture of the passivation film, and then aggravated the corrosion of ST. The concentration of  $\text{Cl}^-$  in PBS solution is the lowest among the four solutions. So, the local rupture in PBS was relatively mild. In addition, both PBS and SBF contain phosphate ions, calcium ions. These ions entered the passivation film during the process of the depassivation and repassivation of titanium element, causing the structure changes of the passivation film and reinforcing the protection of the passivation film [34].

**Table 2.** Fitting results of potentiodynamic polarization tests for ST and CT in the four solutions.

| Sample | Solution              | $E_{\text{corr}}/\text{V}$ | $j_{\text{corr}}/\mu\text{A cm}^{-2}$ | $\beta_a/\text{V}$ | $\beta_c/\text{V}$ | $E_p/\text{V}$ | $i_p/\mu\text{A cm}^{-2}$ |
|--------|-----------------------|----------------------------|---------------------------------------|--------------------|--------------------|----------------|---------------------------|
| ST     | 3.5wt.% NaCl solution | −0.292                     | $2.511 \pm 0.036$                     | 114.8              | −109.5             | 0.279          | 136                       |
|        | 15wt.% NaCl solution  | −0.563                     | $7.065 \pm 0.041$                     | 179.3              | −156.2             | -              | -                         |
|        | PBS buffer solution   | −0.189                     | $1.780 \pm 0.025$                     | 115.6              | −154.3             | 0.233          | 105                       |
|        | SBF solution          | −0.225                     | $2.433 \pm 0.029$                     | 164.4              | −189.2             | 0.247          | 124                       |
| CT     | 3.5wt.% NaCl solution | −0.547                     | $1.493 \pm 0.031$                     | 146.7              | −154.6             | 0.020          | 41.6                      |
|        | 15wt.% NaCl solution  | −0.708                     | $5.972 \pm 0.027$                     | 98.97              | −138.4             | -              | -                         |
|        | PBS buffer solution   | −0.470                     | $1.019 \pm 0.033$                     | 131.0              | −113.5             | −0.0836        | 69.8                      |
|        | SBF solution          | −0.497                     | $1.085 \pm 0.037$                     | 122.8              | −94.41             | 0.0503         | 89.9                      |

The EIS measurements were carried out to investigate the surface conditions of ST and CT immersed in the four solutions, and the relevant Nyquist plots are shown in Figure 4. All the Nyquist plots exhibit only a big capacitive loop for each sample, and the radii of the capacitive loops for CT are larger than that for ST in all solutions. Generally, the large radius of the capacitive loop in the Nyquist plot indicates the difficulty in the electron transfer between solution and substrate [33]. Therefore, the impedance of the formed passive film on CT was higher than that on ST irrespective of the kind of the solution. The equivalent circuit (Figure 5) was used to fit the EIS results, where  $R_s$  is the solution resistance; CPE is the solution double-layer capacitance;  $R_{ct}$  corresponds to the charge transfer resistance. Zsimpwin software was used to fit the test data and the fitted results are summarized in Table 3. Accordingly, in the same solution, the value of  $R_{ct}$  for ST is much lower than that for CT, which indicates the passive films formed on CT possess superior corrosive resistance. The similar conclusion had been demonstrated as SLM-produced Ti6Al4V sheets were immersed in Hanks' solution [21]. The values of  $R_{ct}$  for ST in the four solutions are in the order:  $17.9 \text{ k}\Omega \text{ cm}^{-2}$  (in 15 wt.% NaCl) <  $25.2 \text{ k}\Omega \text{ cm}^{-2}$  (in 3.5 wt.% NaCl) <  $28.1 \text{ k}\Omega \text{ cm}^{-2}$  (in SBF) <  $39.8 \text{ k}\Omega \text{ cm}^{-2}$  (in PBS). This suggests that ST had the best corrosion resistance in PBS. This is in accordance with the results of the potentiodynamic polarization. Furthermore, the parameter of  $n$  is the dispersion constant, and the larger value of  $n$  means a denser passivation film. In the four solutions, CT always possess the values of  $n$  closer to 1 than ST, indicating the passivation films on CT were denser than that on ST, and the films on CT can provide better corrosion resistance.

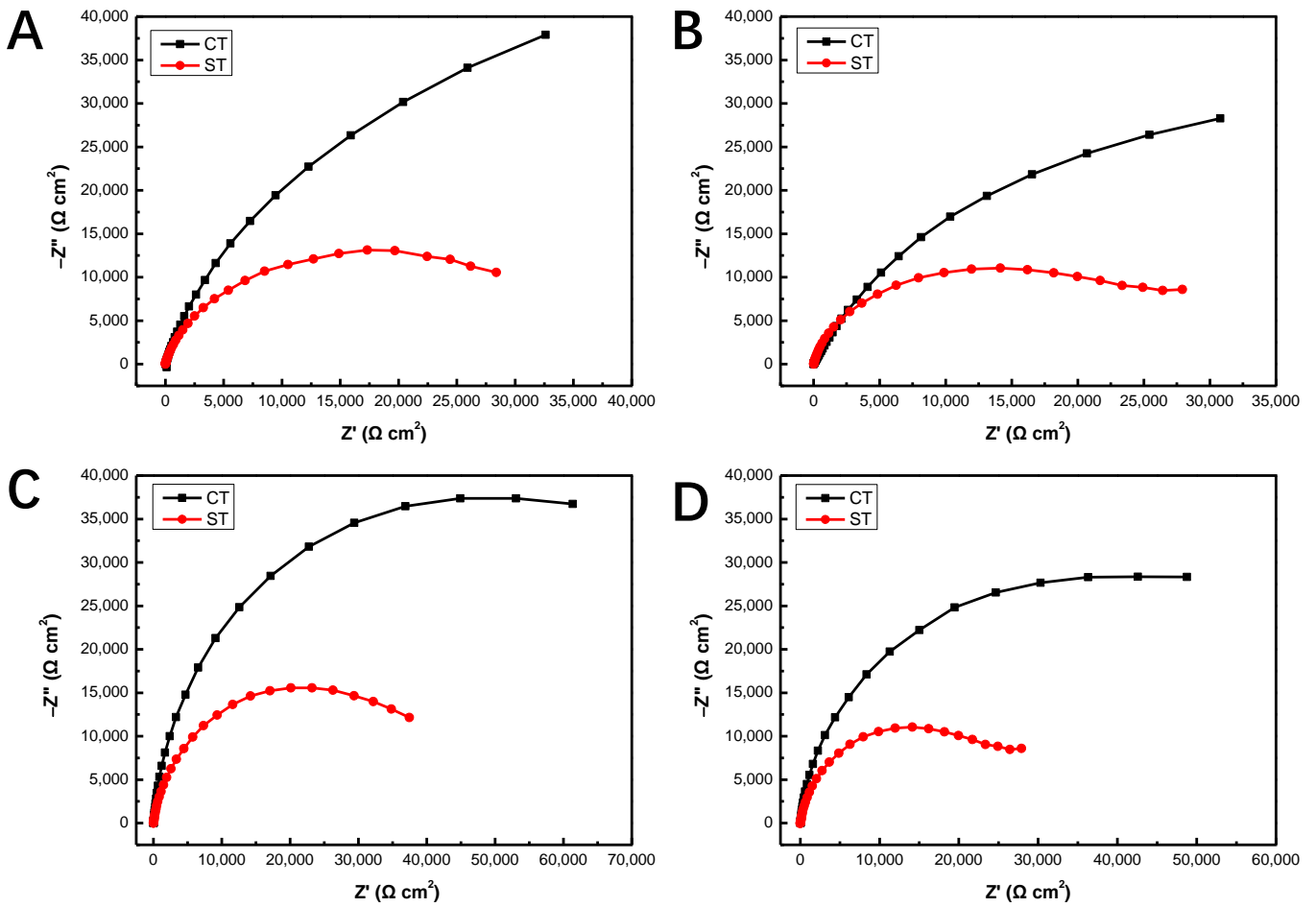


Figure 4. Nyquist plots for ST and CT in (A) 3.5 wt.% NaCl solution, (B) 15 wt.% NaCl solution, (C) PBS buffer solution and (D) SBF solution.

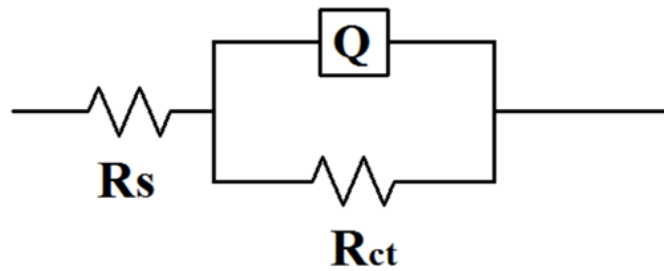


Figure 5. Equivalent circuit used for impedance spectra analysis for ST and CT in the four solutions.

Table 3. Fitting results of EIS tests for ST and CT in the four solutions.

| Sample | Solution              | $R_s/(\Omega \text{ cm}^{-2})$ | $Y_0 \times 10^{-4}/(\text{S Sec}^n \text{ cm}^{-2})$ | n    | $R_{ct}/(\text{k}\Omega \text{ cm}^{-2})$ |
|--------|-----------------------|--------------------------------|---|------|---|
| ST     | 3.5wt.% NaCl solution | $7.86 \pm 1.76$                | 1.06  | 0.87 | $25.2 \pm 0.4$                            |
|        | 15wt.% NaCl solution  | $16.8 \pm 1.93$                | 1.85  | 0.83 | $17.9 \pm 0.2$                            |
|        | PBS buffer solution   | $28.4 \pm 2.58$                | 0.80  | 0.88 | $39.8 \pm 0.1$                            |
|        | SBF solution          | $22.6 \pm 2.40$                | 0.78  | 0.89 | $28.1 \pm 0.2$                            |
| CT     | 3.5wt.% NaCl solution | $8.61 \pm 3.11$                | 0.93  | 0.93 | $36.8 \pm 0.3$                            |
|        | 15wt.% NaCl solution  | $13.4 \pm 2.79$                | 1.93  | 0.85 | $21.3 \pm 0.1$                            |
|        | PBS buffer solution   | $27.9 \pm 2.82$                | 0.97  | 0.93 | $84.0 \pm 0.1$                            |
|        | SBF solution          | $24.3 \pm 1.65$                | 1.16  | 0.93 | $63.4 \pm 0.2$                            |

#### 4. Conclusions

Based on the promising applications of ST, we evaluated the corrosion performances of ST in the four solutions using the potentiodynamic and EIS measurements. We found that CT always presented better corrosion resistance than ST regardless of the kind of solution. This was mainly caused by the differences in the phase composition of the two samples. In ST a considerably large amount of  $\alpha'$  acicular martensitic phases were found. The acicular  $\alpha'$  phase is metastable and possesses the “higher energy state” regarding corrosion, leading to the easy dissolution of  $\alpha'$ -Ti. For the four solutions, PBS signified the highest solution resistance, and ST possessed the largest charge transfer resistance in PBS. This suggests passivation films formed on ST in PBS had the best corrosion resistance.

**Author Contributions:** Conceptualization, Q.L. and Q.F.; methodology, X.C.; software, X.C.; validation, M.G.; formal analysis, X.C.; investigation, X.C.; resources, Q.L.; data curation, X.C.; writing—original draft preparation, X.C.; writing—review and editing, Q.F.; visualization, Q.L.; supervision, Q.L.; project administration, Q.F.; funding acquisition, Q.F. All authors have read and agreed to the published version of the manuscript.

**Funding:** The work was funded by [the National Natural Science Foundation of China] grant number [51902216], [Project of Department of Science and Technology of Sichuan Province] grant number [2022NSFSC0033], [Project of Vanadium and Titanium Resource Comprehensive Utilization Key Laboratory of Sichuan Province] grant number [2018FTSZ06].

**Data Availability Statement:** Data is unavailable due to privacy.

**Conflicts of Interest:** The authors declare no conflict of interest.

#### References

1. Sibum, H.; Güther, V.; Roidl, O.; Habashi, F.; Uwe Wolf, H.; Siemers, C. Titanium, Titanium Alloys, and Titanium Compounds. In *Ullmann's Encyclopedia of Industrial Chemistry*; Bohnet, M., Ed.; Wiley-VCH Publishing: Weinheim, Germany, 2003; pp. 1–35.
2. Ory, F.; Fraysse, J.L. 1.4—Titanium and titanium alloys: Materials, review of processes for orthopedics and a focus on a proprietary approach to producing cannulated bars for screws and nails for trauma. In *Titanium in Medical and Dental Applications*; Froes, F.H., Qian, M., Eds.; Woodhead Publishing: Sawston, UK, 2018; pp. 65–91.
3. Kityk, A.; Protsenko, V.; Danilov, F.; Bobrova, L.; Hnatko, M.; Pavlik, V.; Šoltýs, J.; Labudová, M.; Rusková, M.; Pangallo, D. Design of Ti-6Al-4V alloy surface properties by galvanostatic electrochemical treatment in a deep eutectic solvent Ethaline. *Surf. Coat. Technol.* **2022**, *429*, 127936. [[CrossRef](#)]
4. Liu, S.; Shin, Y.C. Additive manufacturing of Ti6Al4V alloy: A review. *Mater. Des.* **2019**, *164*, 107552. [[CrossRef](#)]
5. Fu, Q.; Hong, Y.; Liu, X.; Fan, H.; Zhang, X. A hierarchically graded bioactive scaffold bonded to titanium substrates for attachment to bone. *Biomaterials* **2011**, *32*, 7333–7346. [[CrossRef](#)]
6. Chen, Y.; Frith, J.E.; Dehghan-Manshadi, A.; Attar, H.; Kent, D.; Soro, N.D.M.; Bermingham, M.J.; Dargusch, M.S. Mechanical properties and biocompatibility of porous titanium scaffolds for bone tissue engineering. *J. Mech. Behav. Biomed. Mater.* **2017**, *75*, 169–174. [[CrossRef](#)] [[PubMed](#)]
7. Tang, H.P.; Wang, J.; Qian, M. 28—Porous titanium structures and applications. In *Titanium Powder Metallurgy*; Qian, M., Froes, F.H., Eds.; Butterworth-Heinemann: Boston, MA, USA, 2015; pp. 533–554.
8. Reig, L.; Amigó, V.; Busquets, D.J.; Calero, J.A. Development of porous Ti6Al4V samples by microsphere sintering. *J. Mater. Process. Technol.* **2012**, *212*, 3–7. [[CrossRef](#)]
9. He, G.; Liu, P.; Tan, Q. Porous titanium materials with entangled wire structure for load-bearing biomedical applications. *J. Mech. Behav. Biomed. Mater.* **2012**, *5*, 16–31. [[CrossRef](#)] [[PubMed](#)]
10. Jia, J.; Siddiq, A.R.; Kennedy, A.R. Porous titanium manufactured by a novel powder tapping method using spherical salt bead space holders: Characterisation and mechanical properties. *J. Mech. Behav. Biomed. Mater.* **2015**, *48*, 229–240. [[CrossRef](#)]
11. Tofail, S.A.M.; Koumoulos, E.P.; Bandyopadhyay, A.; Bose, S.; O'Donoghue, L.; Charitidis, C. Additive manufacturing: Scientific and technological challenges, market uptake and opportunities. *Mater. Today* **2018**, *21*, 22–37. [[CrossRef](#)]
12. Leary, M. Chapter 1—Introduction to AM. In *Design for Additive Manufacturing*; Leary, M., Ed.; Elsevier Publishing: AE Amsterdam, The Netherlands, 2020; pp. 1–6.
13. Ngo, T.D.; Kashani, A.; Imbalzano, G.; Nguyen, K.T.Q.; Hui, D. Additive manufacturing (3D printing): A review of materials, methods, applications and challenges. *Compos. Part B Eng.* **2018**, *143*, 172–196. [[CrossRef](#)]
14. Yadroitsev, I.; Smurov, I. Selective laser melting technology: From the single laser melted track stability to 3D parts of complex shape. *Phys. Procedia* **2010**, *5*, 551–560. [[CrossRef](#)]
15. Fan, Z.; Lu, M.; Huang, H. Selective laser melting of alumina: A single track study. *Ceram. Int.* **2018**, *44*, 9484–9493. [[CrossRef](#)]

16. Sing, S.L.; Wiria, F.E.; Yeong, W.Y. Selective laser melting of lattice structures: A statistical approach to manufacturability and mechanical behavior. *Robot. Comput.-Integr. Manuf.* **2018**, *49*, 170–180. [[CrossRef](#)]
17. Chiu, T.-M.; Mahmoudi, M.; Dai, W.; Elwany, A.; Liang, H.; Castaneda, H. Corrosion assessment of Ti-6Al-4V fabricated using laser powder-bed fusion additive manufacturing. *Electrochim. Acta* **2018**, *279*, 143–151. [[CrossRef](#)]
18. Masoomi, M.; Thompson, S.M.; Shamsaei, N. Laser powder bed fusion of Ti-6Al-4V parts: Thermal modeling and mechanical implications. *Int. J. Mach. Tools Manuf.* **2017**, *118*, 73–90. [[CrossRef](#)]
19. Dai, N.; Zhang, L.-C.; Zhang, J.; Chen, Q.; Wu, M. Corrosion behavior of selective laser melted Ti-6Al-4V alloy in NaCl solution. *Corros. Sci.* **2016**, *102*, 484–489. [[CrossRef](#)]
20. Nicoletto, G. Anisotropic high cycle fatigue behavior of Ti-6Al-4V obtained by powder bed laser fusion. *Int. J. Fatigue* **2017**, *94*, 255–262. [[CrossRef](#)]
21. Cui, Y.-W.; Chen, L.-Y.; Qin, P.; Li, R.; Zang, Q.; Peng, J.; Zhang, L.; Lu, S.; Wang, L.; Zhang, L.-C. Metastable pitting corrosion behavior of laser powder bed fusion produced Ti-6Al-4V in Hank's solution. *Corros. Sci.* **2022**, *203*, 110333. [[CrossRef](#)]
22. Macallister, N.; Vanmeensel, K.; Becker, T.H. Fatigue crack growth parameters of Laser Powder Bed Fusion produced Ti-6Al-4V. *Int. J. Fatigue* **2021**, *145*, 106100. [[CrossRef](#)]
23. Ter Haar, G.M.; Becker, T.H. Laser powder bed fusion produced Ti-6Al-4V: Influence of high-energy process parameters on in-situ martensite decomposition and prior beta grain texture. *J. Alloys Compd.* **2022**, *918*, 165497. [[CrossRef](#)]
24. Chen, Z.; Wu, X.; Davies, C.H.J. Process variation in Laser Powder Bed Fusion of Ti-6Al-4V. *Addit. Manuf.* **2021**, *41*, 101987. [[CrossRef](#)]
25. Brown, D.W.; Anghel, V.; Balogh, L.; Clausen, B.; Johnson, N.S.; Martinez, R.M.; Pagan, D.C.; Rafailov, G.; Ravkov, L.; Strantza, M.; et al. Evolution of the Microstructure of Laser Powder Bed Fusion Ti-6Al-4V During Post-Build Heat Treatment. *Metall. Mater. Trans. A* **2021**, *52*, 5165–5181. [[CrossRef](#)]
26. Ataee, A.; Li, Y.; Brandt, M.; Wen, C. Ultrahigh-strength titanium gyroid scaffolds manufactured by selective laser melting (SLM) for bone implant applications. *Acta Mater.* **2018**, *158*, 354–368. [[CrossRef](#)]
27. Vrancken, B.; Thijs, L.; Kruth, J.P.; Van Humbeeck, J. Microstructure and mechanical properties of a novel  $\beta$  titanium metallic composite by selective laser melting. *Acta Mater.* **2014**, *68*, 150–158. [[CrossRef](#)]
28. Oyane, A.; Kim, H.-M.; Furuya, T.; Kokubo, T.; Miyazaki, T.; Nakamura, T. Preparation and assessment of revised simulated body fluids. *J. Biomed. Mater. Res. Part A* **2003**, *65A*, 188–195. [[CrossRef](#)]
29. Bai, Y.; Gai, X.; Li, S.; Zhang, L.-C.; Liu, Y.; Hao, Y.; Zhang, X.; Yang, R.; Gao, Y. Improved corrosion behaviour of electron beam melted Ti-6Al-4V alloy in phosphate buffered saline. *Corros. Sci.* **2017**, *123*, 289–296. [[CrossRef](#)]
30. Zhao, X.L.; Li, S.J.; Zhang, M.; Liu, Y.D.; Sercombe, T.B.; Wang, S.G.; Hao, Y.L.; Yang, R.; Murr, L.E. Comparison of the microstructures and mechanical properties of Ti-6Al-4V fabricated by selective laser melting and electron beam melting. *Mater. Des.* **2016**, *95*, 21–31. [[CrossRef](#)]
31. Safdar, A.; Wei, L.Y.; Snis, A.; Lai, Z. Evaluation of microstructural development in electron beam melted Ti-6Al-4V. *Mater. Charact.* **2012**, *65*, 8–15. [[CrossRef](#)]
32. Yadroitsev, I.; Krakhmalev, P.; Yadroitsava, I. Selective laser melting of Ti6Al4V alloy for biomedical applications: Temperature monitoring and microstructural evolution. *J. Alloy. Compd.* **2014**, *583*, 404–409. [[CrossRef](#)]
33. Dai, N.; Zhang, L.-C.; Zhang, J.; Zhang, X.; Ni, Q.; Chen, Y.; Wu, M.; Yang, C. Distinction in corrosion resistance of selective laser melted Ti-6Al-4V alloy on different planes. *Corros. Sci.* **2016**, *111*, 703–710. [[CrossRef](#)]
34. Gudić, S.; Vrsalović, L.; Kvrđić, D.; Nagode, A. Electrochemical Behaviour of Ti and Ti-6Al-4V Alloy in Phosphate Buffered Saline Solution. *Materials* **2021**, *14*, 7495. [[CrossRef](#)]

**Disclaimer/Publisher's Note:** The statements, opinions and data contained in all publications are solely those of the individual author(s) and contributor(s) and not of MDPI and/or the editor(s). MDPI and/or the editor(s) disclaim responsibility for any injury to people or property resulting from any ideas, methods, instructions or products referred to in the content.